nature energy

Article

https://doi.org/10.1038/s41560-024-01565-z

Towards long-life 500 Wh kg^{-1} lithium metal pouch cells via compact ion-pair aggregate electrolytes

Received: 15 August 2023

Accepted: 30 May 2024

Published online: 08 July 2024

Check for updates

Yulin Jie[1,11], Shiyang Wang[2,11], Suting Weng[3,11], Yue Liu[4,11], Ming Yang[5], Chao Tang[1,6], Xinpeng Li[1], Zhengfeng Zhang[7], Yuchen Zhang[1], Yawei Chen[1], Fanyang Huang[1], Yaolin Xu[8], Wanxia Li[1], Youzhang Guo[1], Zixu He[1], Xiaodi Ren[1], Yuhao Lu[6], Ke Yang[9], Saichao Cao[9], He Lin[9], Ruiguo Cao[1], Pengfei Yan[7], Tao Cheng[4] ✉, Xuefeng Wang[3,10] ✉, Shuhong Jiao[1] ✉ & Dongsheng Xu[2] ✉

The development of practical lithium metal cells is plagued by their limited lifespan, primarily due to the poor interfacial stability of the electrolytes. Here we present a compact ion-pair aggregate (CIPA) electrolyte that enables high-performance Li metal pouch cells under lean electrolyte conditions. The electrolyte features a unique nanometre-scale solvation structure in which ion pairs are densely packed to form large CIPAs, in contrast to conventional electrolytes that comprise small aggregates. Notably, the CIPAs facilitate fast interfacial reduction kinetics on the Li metal anode via a collective electron-transfer process, leading to the formation of a stable interface. A 505.9 Wh kg^{-1} Li metal pouch cell with a high-nickel-content cathode ($LiNi_{0.905}Co_{0.06}Mn_{0.035}O_2$) exhibited a 91% energy retention after 130 cycles. This work demonstrates nanostructured electrolyte design for realizing high-performance Li metal batteries. It also showcases the importance of understanding interfacial reaction mechanisms in the design and development of electrolytes.

Lithium metal batteries (LMBs) are receiving intense interest because of their high energy densities (>500 Wh kg^{-1})[1]. However, their commercialization is impeded by their limited lifespan under lean electrolyte conditions (electrolyte mass/cell capacity (*E*/*C*) ratio < 3 g Ah^{-1})[2]. Electrolyte design plays an essential role in improving LMB lifespan by tuning the compositions and structures of the solid–electrolyte interphase (SEI) and cathode–electrolyte interphase[3–6]. For high-voltage LMBs with a transition metal oxide cathode, designing a highly compatible electrolyte remains a formidable challenge because both the anode and cathode operate at extreme voltages with high interfacial reactivity (−3.04 and >1.25 V versus the standard hydrogen electrode for the anode and cathode, respectively). Although excellent interfacial stability of the anode or cathode can be achieved in certain electrolytes, this often compromises the stability of the counterpart. For instance, a carbonate electrolyte has been demonstrated to achieve high cathode Coulombic efficiencies (CEs) of up to >99.99%, but it is typically unstable with the Li metal anode[7,8], whereas an ether electrolyte composed of 1 M lithium bis(fluorosulfonyl)imide–1,3-dioxolane + 4 wt% $LiNO_3$ exhibits a high anode CE of 99.7%, but its poor oxidative stability renders it incompatible with high-voltage cathodes[9]. Despite substantial progress in the development of electrolytes for LMBs, such as high concentration electrolytes[10,11], liquefied gas electrolytes[12–14] and weakly solvating electrolytes[5,15], further improvements in both anode and cathode interfaces are highly demanded.

Recently, localized high-concentration electrolytes (LHCEs) have emerged as promising candidates for stabilizing both anode

A full list of affiliations appears at the end of the paper. ✉e-mail: tcheng@suda.edu.cn; wxf@iphy.ac.cn; jiaosh@ustc.edu.cn; dsxu@pku.edu.cn

and cathode interfaces in high-voltage LMBs[16–18]. Subsequent advances in the electrolyte design, such as solvent optimization[19,20] and diluent selection[21,22], have further verified the capability of LHCEs to enable stable high-voltage LMBs. Nevertheless, a comprehensive mechanistic understanding of LHCEs, particularly regarding their solvation structure, remains elusive, hindering further improvement. Research interest has predominantly focused on the first solvation sheath, while the features of extended-scale structures remain largely unknown[23,24]. Furthermore, their interfacial reaction mechanisms are less explored, despite their pivotal role in bridging the knowledge gap between SEI composition/structure and solvation structure.

Here we report a compact ion-pair aggregate (CIPA) electrolyte designed to stabilize both the anode and high-voltage cathode interfaces, enabling the stable cycling of 500 Wh kg^{-1} Li metal pouch cells. The solvation structures and interfacial reaction mechanisms of the CIPA electrolyte and conventional LHCEs are illustrated in Fig. 1a. The CIPA electrolyte consists of large aggregates (AGGs; 3–4 nm in size) at the mesoscopic scale, where ion pairs are densely packed together, leading to short Li^+–Li^+ distances of ~6 Å. In contrast, conventional LHCEs typically contain small AGGs (~1 nm in size) with large Li^+–Li^+ distances of ~8 Å. Notably, the CIPA electrolyte undergoes a unique interfacial reaction mechanism via a collective reduction process, forming a stable SEI with a high inorganic content and a small average thickness of ~6.2 nm. Additionally, the CIPA electrolyte effectively stabilizes the cathode material by suppressing irreversible interfacial change. Consequently, the CIPA electrolyte enables the stable cycling of 505.9 Wh kg^{-1} Li metal pouch cells over 130 cycles.

Evaluation of electrolyte in Li metal pouch cells

We first evaluated the CIPA electrolyte and conventional LHCEs in 500 Wh kg^{-1} Li metal pouch cells with a $LiNi_{0.905}Co_{0.06}Mn_{0.035}O_2$ (Ni90) cathode under lean electrolyte conditions ($E/C \approx 1.25$ g Ah^{-1}; Fig. 1b). The energy density was calculated on the basis of the total weight of the cell, including packaging (see Fig. 1c and Supplementary Table 1 for details of the cell parameters). The CIPA electrolyte was prepared by dissolving 2 M lithium bis(fluorosulfonyl)imide (LiFSI) in a 1:1 mixture (by volume) of ethylene glycol di-*n*-butyl ether (EGBE) and 1,1,2,2-tetrafluoroethyl 2,2,3,3-tetrafluoropropyl ether (TTE). Conventional LHCEs were prepared using LiFSI, TTE and 1,2-dimethoxyethane (DME) or triethylene glycol dimethyl ether (G3), denoted LHCE-DME and LHCE-G3, respectively, for comparison. Supplementary Figs. 1 and 2 show that all three electrolytes have comparable viscosity (9–20 mPa·s) and maintain a liquid state over a wide temperature range (−20 to 80 °C).

Figure 1b shows the long-term cycling performance of Li metal pouch cells prepared with the different electrolytes at a charge/discharge rate of 0.1 C/0.1 C. The pouch cells with the LHCE-DME and LHCE-G3 electrolytes exhibited a rapid loss of capacity and failure after 56 and 77 cycles, respectively. Notably, the LHCE-DME electrolyte caused severe swelling of the cell during long-term cycling, leading to serious safety concerns (Supplementary Fig. 3). In sharp contrast, the cell with the CIPA electrolyte achieved a cycle life of 130 cycles (~2,750 h) with a high energy retention of 91%, twice that of the cells with the conventional LHCEs. Moreover, the average CE with the CIPA electrolyte reached 99.94% over the 130 cycles (Supplementary Fig. 4), greater than that of the LHCE-DME and LHCE-G3 electrolytes (99.53% and 99.55%, respectively). We further evaluated the CIPA electrolyte at an increased charge cut-off voltage up to 4.4 V. As shown in Supplementary Fig. 5, the pouch cell with a high cut-off voltage delivered a higher energy density of 520.3 Wh kg^{-1} with a high energy retention of 95% after 100 cycles. We also evaluated pouch cells with a lower energy density (423.7 Wh kg^{-1}; the cell parameters are shown in Supplementary Table 2) at a higher discharge rate (0.1 C/0.5 C). The pouch cell with the CIPA electrolyte achieved a long lifespan of 300 cycles (Supplementary Fig. 6), three times higher than that with the LHCE-G3 electrolyte (<100 cycles). Remarkably, the CIPA electrolyte exhibited a high capacity retention (93%) and average CE (99.91%; Supplementary Fig. 7), along with a stable average voltage (Supplementary Fig. 8). These results indicate that the CIPA electrolyte improves the interfacial stability of the highly active Li metal anode and high-voltage cathode, rendering Li metal pouch cells with remarkable performance under lean electrolyte conditions.

The performances of high-voltage Li metal pouch cells in terms of energy density and cycle number/time reported in the recent literature[8,15,25–45] and those of our CIPA-based pouch cells are presented in Fig. 1d, Supplementary Fig. 9 and Supplementary Table 3. Notably, a trade-off between energy density and cycle number is clearly demonstrated in Fig. 1d. The cycle number of lithium metal pouch cells is significantly compromised by a high energy density. Previous studies showed that few Li metal pouch cells with an energy density of 500 Wh kg^{-1} maintained a stable performance beyond 50 cycles. In contrast, the Li metal pouch cell with the CIPA electrolyte achieved up to 130 cycles during long-term cycling with 100% depth of discharge, which is considerably higher than the previously reported highest value. Furthermore, the correlation between cycle number and E/C ratio in Li metal pouch cells exhibits a comparable trend (Supplementary Fig. 10). Lean electrolyte conditions (lower E/C ratio) significantly accelerate the electrolyte depletion process, leading to rapid cell degradation and short cycling lifespans. Remarkably, Li metal pouch cells with the CIPA electrolyte could achieve over 300 stable cycles, even when operating under ultra-lean electrolyte conditions with an E/C ratio as low as 1.25 g Ah^{-1} (Supplementary Fig. 10), thereby marking a state-of-the-art advance.

Interfacial characterization and analysis

To investigate the underlying mechanism responsible for the discrepancies in pouch cell performance, we evaluated the electrolytes in coin-type cells and conducted thorough characterizations of both the Li metal anode and high-voltage cathode. Notably, Li||Cu coin cells with the CIPA electrolyte achieved approximately twofold longer cycle life (400 cycles) and a higher average CE than those with the LHCE-G3 electrolyte (Fig. 2a,b and Supplementary Fig. 11). In addition, a high average CE of 99.5% was achieved with the CIPA electrolyte in further electrochemical test (Supplementary Fig. 12), indicating the formation of a highly stable anode interface. Furthermore, Li||$LiNi_{0.8}Co_{0.1}Mn_{0.1}O_2$ (NCM811) cells with the CIPA electrolyte delivered a high capacity retention of 99.4% over 300 cycles (Supplementary Fig. 13) with a remarkable average CE of 99.99%. The excellent interfacial stability of both the anode and cathode effectively mitigates the electrolyte depletion caused by parasitic reactions, underlying the outstanding performance of the LMBs under ultra-lean electrolyte conditions. Supplementary Fig. 14 shows comparable rate capability for both the CIPA and LHCE-G3 electrolytes.

To investigate the stability of the solvent on the high-voltage cathode side, the cross-section morphology and interfacial phase transition of the NCM811 electrode were characterized after long-term cycling in LiFSI–EGBE and LiFSI–G3 electrolytes. Focused ion beam scanning electron microscopy (FIB-SEM) characterization showed that the structural integrity of the NCM811 electrode in the LiFSI–EGBE electrolyte was maintained without evident cracks after 200 cycles (Fig. 2c and Supplementary Fig. 15). In contrast, intergranular cracks (marked by arrows) inside the secondary particles were clearly observed in the electrode cycled in the LiFSI–G3 electrolyte (Fig. 2d). Meanwhile, high-angle annular dark-field scanning transmission electron microscopy (HAADF-STEM) revealed that the LiFSI–EGBE electrolyte substantially suppressed the interfacial phase transition, presenting a thin (~2.2 nm) phase-transition layer on the surface of the NCM811 particles (Fig. 2c). In sharp contrast, for the NCM811 electrode cycled in the LiFSI–G3 electrolyte, a significantly thicker phase-transition layer of up to 10.0 nm was observed (Fig. 2d). Gas chromatography–mass spectrometry (GC–MS) and inductively coupled plasma mass spectrometry (ICP-MS) further corroborated the greater stability

https://doi.org/10.1038/s41560-024-01565-z

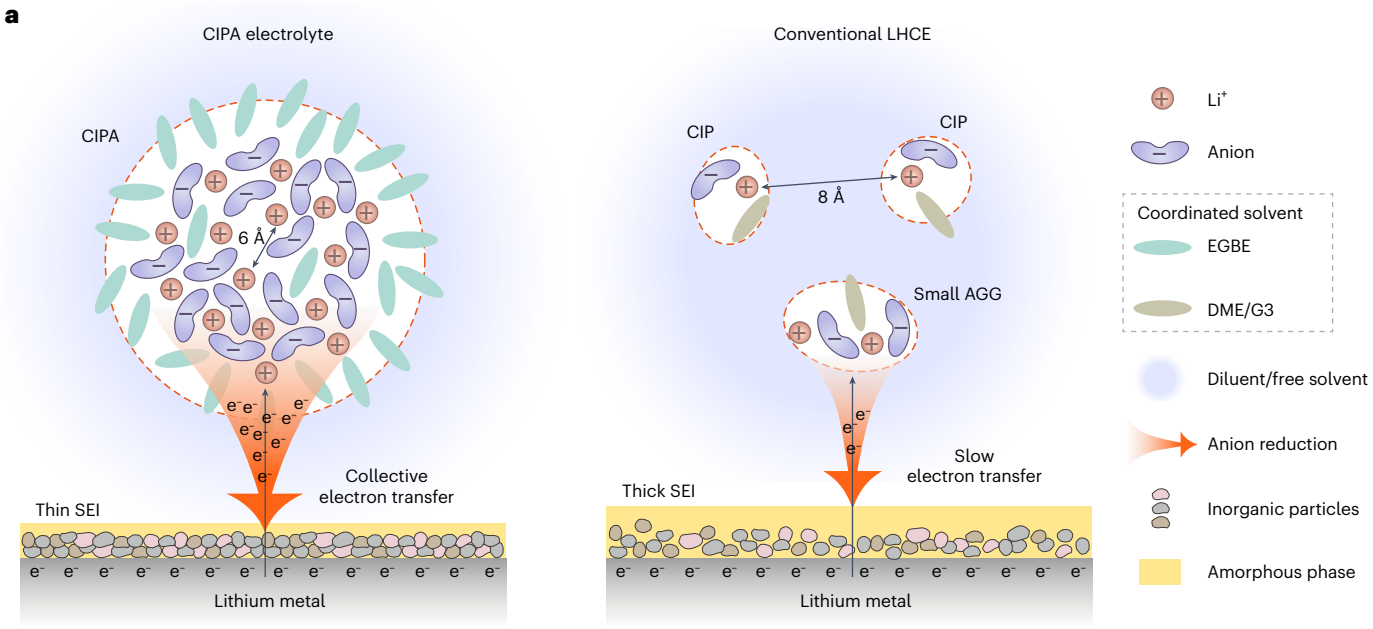

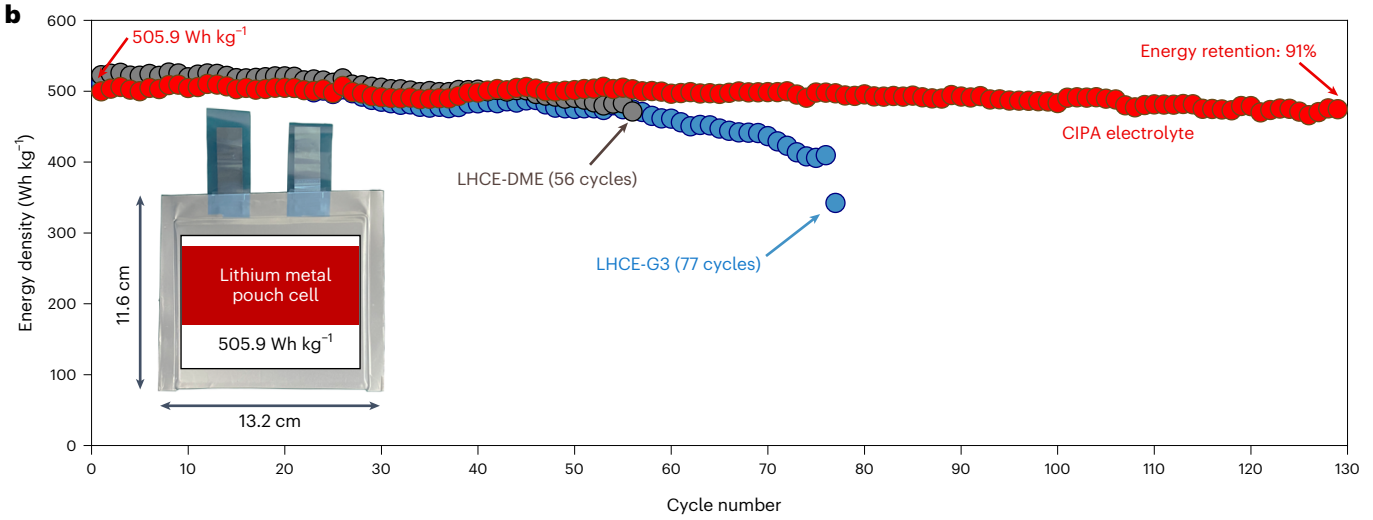

c

Pouch cell parameters	
Electrolyte	*E*/C ratio = 1.25 g Ah^{-1}
Anode	60 μm Li foil
Cathode capacity	~4.2 mAh cm^{-2}
N/*P* ratio	~1.5
Cell weight	142.0 g
Cell capacity	19 Ah
Energy density	505.9 Wh kg^{-1}

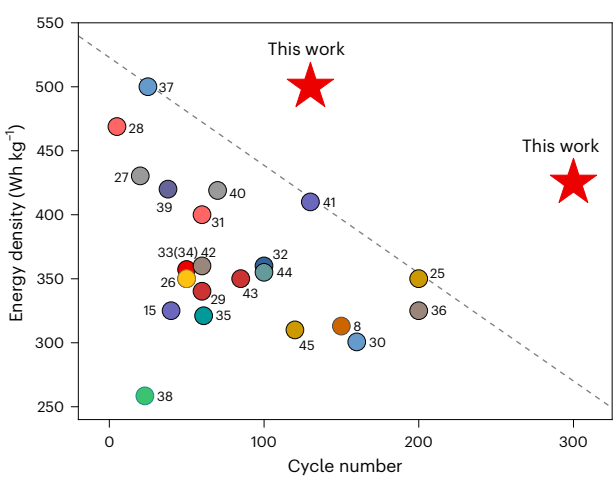

Fig. 1 | Features of the CIPA electrolyte and evaluation of Li metal pouch cells. a, Schematics of the solvation structures and interfacial reaction mechanisms of the CIPA electrolyte and conventional LHCEs. **b**, Long-term cycling performance of >500 Wh kg^{-1} Li metal pouch cells at a voltage of 3.0–4.3 V and a charge/discharge rate of 0.1 C/0.1 C. **c**, Parameters of the 505.9 Wh kg^{-1} Li metal pouch cell. *N*/*P*, negative-to-positive areal capacity. **d**, Energy densities and cycle numbers (at a capacity retention of 90%) of Li metal pouch cells reported in this work and in the literature[8,15,25–45].

https://doi.org/10.1038/s41560-024-01565-z

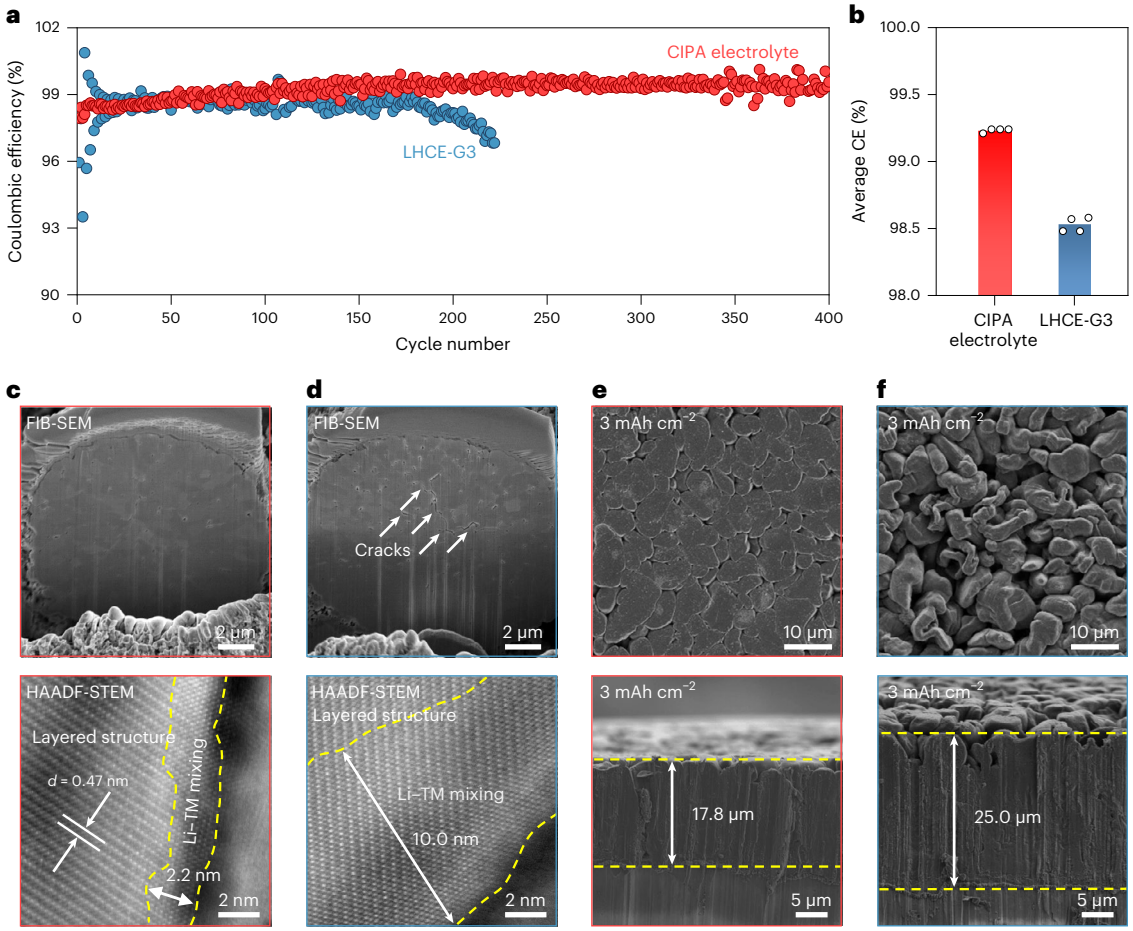

Fig. 2 | Interfacial stability of the Li metal anode and NCM811 cathode. **a**, CEs of Li||Cu coin cells with CIPA and LHCE-G3 electrolytes at a current density of 0.5 mA cm^{-2} and areal capacity of 1 mAh cm^{-2}. **b**, Average CEs of Li||Cu coin cells with CIPA and LHCE-G3 electrolytes at 0.5 mA cm^{-2} and 1 mAh cm^{-2}. The circles represent data from different cells and the heights of the bars represent the means. **c**,**d**, FIB-SEM characterization of cross-section morphologies and HAADF-STEM characterization of the interfaces of the NCM811 cathodes cycled in LiFSI–EGBE (**c**) and LiFSI–G3 (**d**) electrolytes. **e**,**f**, Top-view and cross-section-view SEM images of the Li plating morphologies on Cu substrates in CIPA (**e**) and LHCE-G3 (**f**) electrolytes at a current density of 0.5 mA cm^{-2} and areal capacity of 3 mAh cm^{-2}.

of the NCM811 cathode in the CIPA electrolyte compared with in the LHCE-G3 electrolyte. The CIPA electrolyte mitigated the dissolution of transition metals from the NCM811 cathode and exhibited better oxidative stability with an appreciably decreased production of CO_2 at the cathode interface (Supplementary Figs. 16 and 17). These findings show that the high-voltage NCM811 cathode material has superior stability in the EGBE solvent.

To thoroughly investigate the stability of the electrolyte on the Li metal anode side, the morphology of Li plating was studied by SEM at an areal capacity of 3 mAh cm^{-2}. The top-view images show that the CIPA electrolyte leads to a dendrite-free and planar Li morphology (Fig. 2e), while the LHCE-G3 electrolyte triggers dendritic Li growth (Fig. 2f). The cross-section-view images show that the plated Li formed a dense deposition layer with a thickness of 17.8 μm in the CIPA electrolyte (Fig. 2e), mitigating parasitic reactions and the generation of dead Li on the Li metal anode. In contrast, in the LHCE-G3 electrolyte, a much thicker Li deposition layer was observed (25.0 μm) with a more porous structure and a rougher morphology (Fig. 2f). The Li plating showed the same trend in terms of deposition morphology and layer thickness at the higher capacity of 5 mAh cm^{-2} (Supplementary Figs. 18 and 19).

To understand the underlying reasons for the different deposition behaviours, we used cryogenic transmission electron microscopy (cryo-TEM) combined with advanced surface characterization techniques to thoroughly characterize the composition and structure of the SEIs formed in the two electrolytes. Cryo-TEM revealed that the SEI formed by the CIPA electrolyte on the Li metal surface was thin and conformal, with an average thickness of ~6.2 nm (Fig. 3a and Supplementary Figs. 20–24). In contrast, the average thickness of the SEI formed in the LHCE-G3 electrolyte was ~10.9 nm (Fig. 3b and Supplementary Figs. 25–28), substantially larger than that in the CIPA electrolyte. Notably, Li_2O nanocrystalline domains were observed embedded in the SEIs formed in both electrolytes. Importantly, the Li_2O nanocrystalline domains formed in the CIPA electrolyte were of a more uniform size and with a more homogeneous distribution compared with those formed in the SEI of the LHCE-G3 electrolyte. The homogeneity of the SEI structure plays an essential role in suppressing the dendritic Li growth and improving the reversibility of the Li metal anode.

X-ray photoelectron spectroscopy (XPS) characterization with depth profiling was performed to further explore the compositional structure of the SEIs. Supplementary Fig. 29 shows the composition of the outer surface of the SEIs before sputtering with argon cluster ions. The CIPA electrolyte formed a SEI composed of inorganic compounds, including LiF, Li_2O and Li_2CO_3, as well as organic C–C and C–O species. A smaller LiF peak was observed for the LHCE-G3 electrolyte, suggesting a decreased reduction of FSI^- anions. A stronger LiF signal was also observed in the CIPA electrolyte after sputtering (Fig. 3c and Supplementary Fig. 30).

https://doi.org/10.1038/s41560-024-01565-z

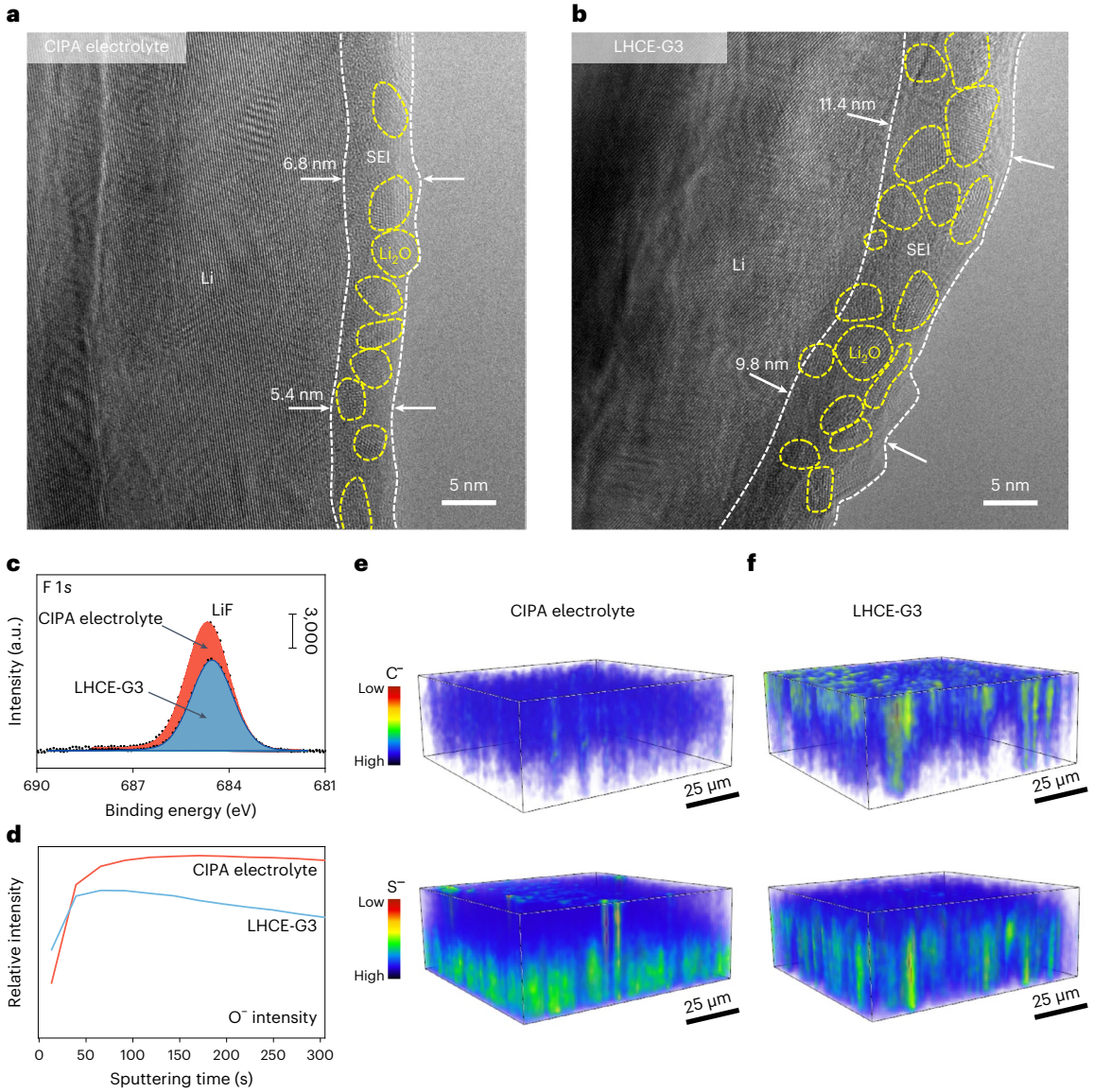

Fig. 3 | Interfacial characterization of the Li metal anode. a,**b**, Cryo-TEM characterization of the structure and morphology of the SEI formed in the CIPA (**a**) and LHCE-G3 (**b**) electrolytes at 0.5 mA cm^{-2} after 30 min. **c**, XPS characterization of the SEIs after argon cluster ion sputtering for 120 s. **d**, TOF-SIMS characterization of the O$^-$ fragments of the SEIs formed in the CIPA and LHCE-G3 electrolytes at 0.5 mA cm^{-2} and 3 mAh cm^{-2}. **e**,**f**, TOF-SIMS three-dimensional depth-profiling images of the C$^-$ and S$^-$ species in the SEIs formed in the CIPA (**e**) and LHCE-G3 (**f**) electrolytes. The colour from black (bottom side) to red (top side) in colour bars represents the gradually increased intensity.

We also used time-of-flight secondary ion mass spectrometry (TOF-SIMS) to investigate the composition of the SEIs and their spatial distribution. We observed a weaker C$^-$ signal in the SEI derived from the CIPA electrolyte than in the SEI from the LHCE-G3 electrolyte, while the O$^-$ signal was stronger in the former (Fig. 3d and Supplementary Figs. 31 and 32). Considering that the carbon comes entirely from the decomposition of the solvent, these results indicate that solvent decomposition is more severe in the LHCE-G3 electrolyte than in the CIPA electrolyte.

TOF-SIMS three-dimensional mapping revealed that the SEI derived from the CIPA electrolyte shows a negligible C$^-$ signal from the bottom to the top across the whole SEI layer (Fig. 3e) and a uniform distribution of the S$^-$ signal in the inner part of the SEI. In contrast, C$^-$ species were clearly detected in the outer part of the SEI derived from the LHCE-G3 electrolyte and S$^-$ species concentrated in the inner part (Fig. 3f). The C$^-$ and S$^-$ signals are less homogeneously distributed in the SEI formed in the LHCE-G3 electrolyte. This suggests a non-uniform reduction behaviour of the LHCE-G3 electrolyte to form inhomogeneous SEIs, which might trigger localized Li deposition leading to the evolution and propagation of Li dendrite.

Insights into electrolyte solvation structures

To unravel the origin of the improved interfacial stability and outstanding electrochemical performance of the cells prepared with the CIPA electrolyte, we comprehensively investigated the solvation structures of the CIPA and LHCE-G3 electrolytes. The mesoscopic solvation structures at the nanometre scale were first examined by molecular dynamics (MD) simulations, focusing on the interactions between the ion pairs that dictate the formation of the AGGs (Fig. 4a,b). No solvents or diluents are shown in the MD snapshots to highlight the ion pairs. Figure 4a shows that the CIPA electrolyte consists of large (3–4 nm in the maximum dimension) and compact AGGs formed by densely packed ion pairs. We define these large compact AGGs as CIPAs. In sharp contrast, small AGGs (~1.2 nm) predominate in the LHCE-G3 electrolyte as a result of the tendency of most ion pairs to isolate (Fig. 4b). A statistical

https://doi.org/10.1038/s41560-024-01565-z

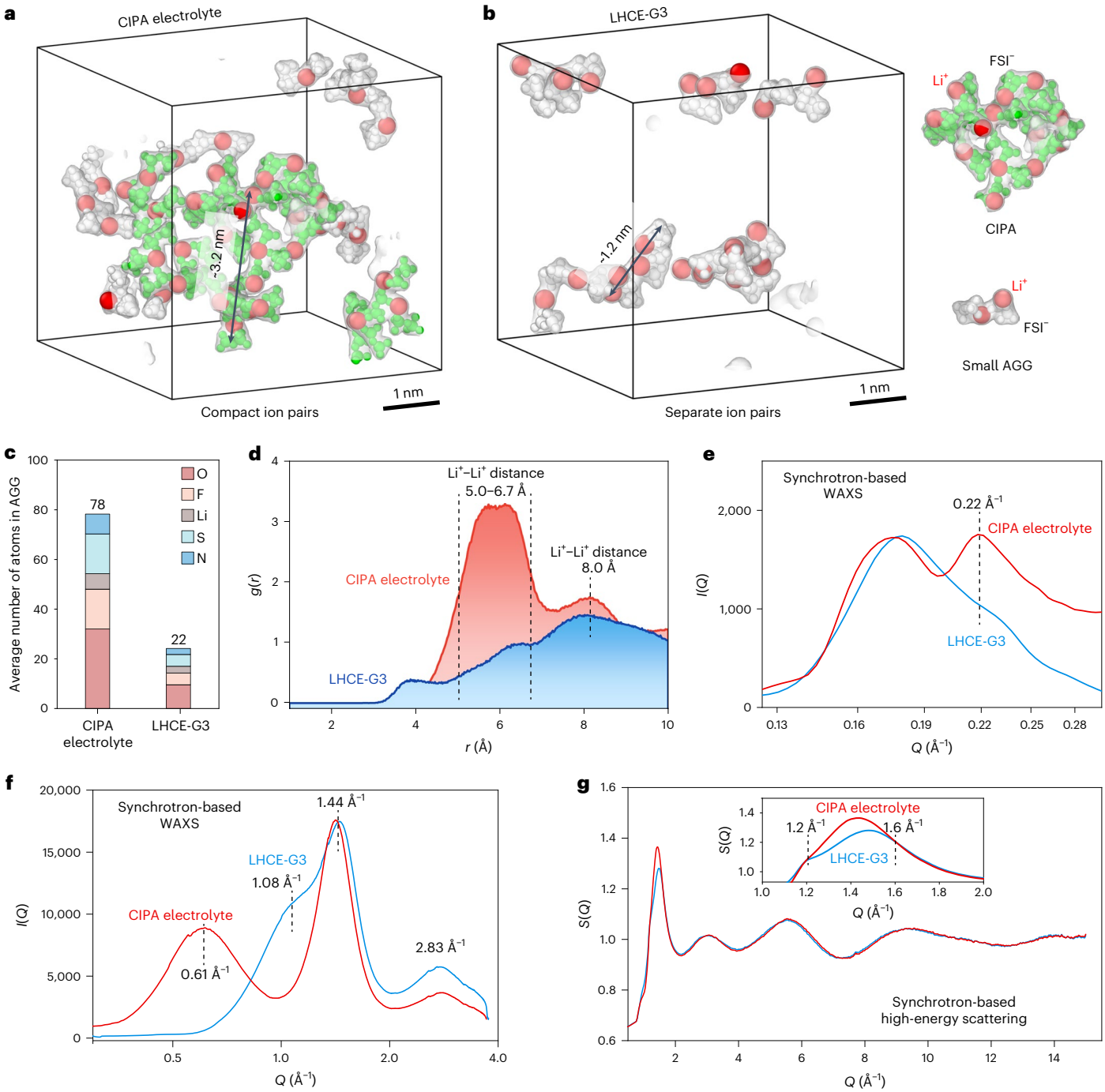

Fig. 4 | Meso- and microscopic solvation structures. a,**b**, MD snapshots of the AGG structures in the CIPA (**a**) and LHCE-G3 (**b**) electrolytes. **c**, Average number of atoms in discrete AGGs in the two electrolytes. **d**, Li^+–Li^+ RDFs ($g(r)$) in the two electrolytes, derived from MD simulations. r represents the distance between Li^+ ions. **e**,**f**, Synchrotron-based WAXS intensity in the low-Q (**e**) and high-Q (**f**) regions for the two electrolytes. **g**, Structure factor functions $S(Q)$ for the two electrolytes, derived from synchrotron-based high-energy X-ray scattering. Insets are provided to show an enlarged view between 1.0 $Å^{-1}$ and 2.0 $Å^{-1}$ for clarity.

analysis of the size of the AGGs (defined as the average number of atoms of all ion pairs in a discrete CIPA or AGG) in the CIPA and LHCE-G3 electrolytes revealed that each CIPA consisted on average of 78 atoms, >3.5-fold higher than the number of atoms (~22 atoms) in each AGG in the LHCE-G3 electrolyte (Fig. 4c). The formation mechanism of the CIPAs was also probed. Detailed solvation structure analysis (Supplementary Figs. 33 and 34) revealed that the CIPAs are uniquely formed through the coordination of multiple ion pairs, further corroborating the densely packed nature of ion pairs in the CIPA electrolyte.

The microscopic solvation structure of the CIPA electrolyte was also analysed by MD simulations. Figure 4d shows the Li^+–Li^+ radial distribution functions (RDFs, $g(r)$) of the CIPA and LHCE-G3 electrolytes. The RDF curve of the CIPA electrolyte exhibits a pronounced peak at 5.0–6.7 Å. However, the LHCE-G3 electrolyte shows no significant peak in this range. The peak at 5.0–6.7 Å arises from the coordination of ion pairs, the distance between two Li^+ ions typically being 5–6 Å (Supplementary Fig. 35). This further demonstrates that a significant proportion of the ion pairs in the CIPA electrolyte are coordinated to

https://doi.org/10.1038/s41560-024-01565-z

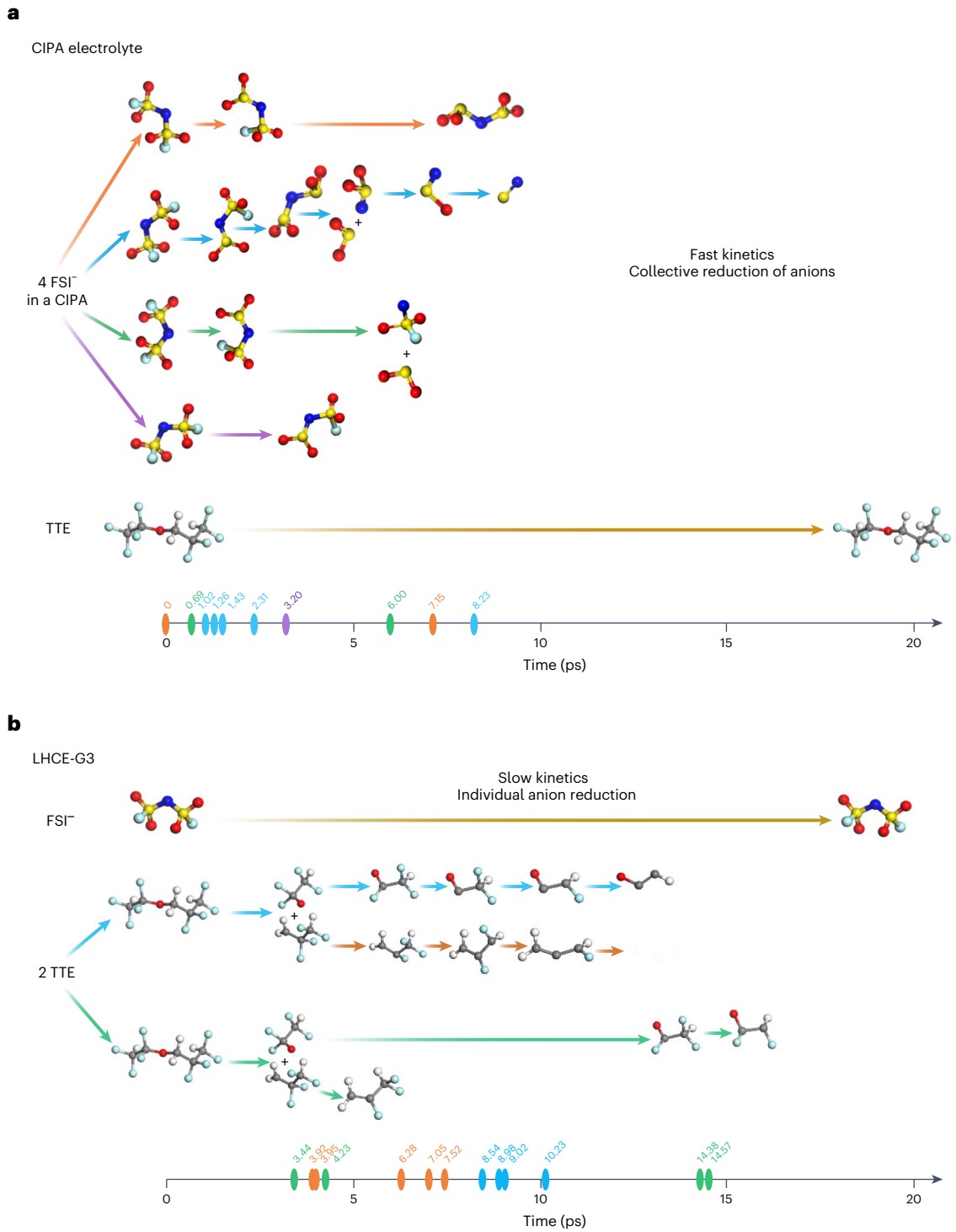

Fig. 5 | Interfacial reaction mechanism. a,**b**, Kinetics and pathways of the reactions of the CIPA (**a**) and LHCE-G3 (**b**) electrolytes on the Li surface, derived from AIMD simulations. The timeline represents the time when electrolyte components and their derivatives undergo reduction in AIMD simulations. The coloured elipses on the axes mark the time of the reduction steps of specific electrolyte components. The colours of the elipses correspond to the colours of the arrows in the reaction pathways. Colour code of the atoms: S, yellow; N, blue; O, red; F, cyan; C, grey; H, white.

each other, facilitating the formation of compact large CIPAs. Thus, the nanoscale structure and atom-to-atom analysis together provide a detailed description of the CIPAs featuring in the CIPA electrolyte. Note that the number of coordinated ion pairs tends to decrease when TTE is removed (Supplementary Fig. 36). Moreover, TTE can substantially reduce the viscosity of electrolytes and subsequently improve their ionic conductivity (Supplementary Fig. 37), as evidenced by the superior electrochemical performance of the CIPA electrolyte compared with its 4 M LiFSI–EGBE counterpart (Supplementary Figs. 38 and 39).

To verify the results of the simulations, we conducted synchrotron-based X-ray scattering experiments, including wide-angle X-ray scattering (WAXS) and high-energy X-ray scattering. The mesoscopic/microscopic structures in the CIPA and conventional LHCE electrolytes were investigated by WAXS with a beam energy of 10 keV.

Figure 4e shows the scattering intensity $I(Q)$ in the low-Q region (0.125–0.300 Å^{-1}), derived from the scattering patterns of the two electrolytes (where Q is the wave vector, given by $4\pi\sin(\theta)/\lambda$, where λ is the wavelength of the incident X-ray beam and θ is half of the scattering angle). For the CIPA electrolyte, a strong peak centred at $Q = 0.22$ Å^{-1} can be observed (corresponding to 3.5 nm, according to the Ehrenfest equation $Q \cdot r = 2.46\pi$, where r is the characteristic interatomic correlation distance)[46], suggesting the existence of large AGGs (~3.5 nm) in the CIPA electrolyte. In contrast, for the LHCE-G3 electrolyte, no peak is detected in the same region, indicating the absence of large AGGs, which is consistent with the simulations. Figure 4f shows the scattering intensity in the high-Q region, corresponding to short-range structural correlations. Three broad peaks can be observed between 0.6 and 3 Å^{-1} in the curves of the CIPA and LHCE-G3 electrolytes. For the CIPA electrolyte, the first peak is centred at 0.61 Å^{-1}, corresponding to $r = 12.7$ Å, while for the LHCE-G3 electrolyte, the first peak emerges at a higher Q value (centred at 1.08 Å^{-1}). High-energy X-ray scattering with a beam energy of 88.6 keV was also conducted to further investigate the short-range structure in the electrolytes. Figure 4g shows the structure factor functions $S(Q)$ of the CIPA and LHCE-G3 electrolytes. For both electrolytes, the first peaks lie in the Q range of 1.2–1.6 Å^{-1}, corresponding to $r = 4.8$–6.4 Å. Notably, the intensity of the CIPA electrolyte peak is appreciably higher than that of the LHCE-G3 electrolyte, indicating stronger interactions between ions in the range of 4.8–6.4 Å, agreeing well with the results of the simulations.

The coordination state and configuration of the solvents were studied by Raman spectroscopy in the range of 800–950 cm^{-1} (Supplementary Fig. 40), where C–O bond vibrational peaks appear (centred at ~850 and 905 cm^{-1}), corresponding to the *gauche* and *trans* configurations, respectively, of the O–C–C–O segment in ether solvents[47]. For the CIPA electrolyte, a blueshift of only the *trans* peaks (905 to 920 cm^{-1}) was observed after adding LiFSI to the EGBE–TTE solution (1:1, v/v). This indicates that EGBE typically coordinates to the Li^+ ions in a *trans* configuration, with each EGBE contributing one O atom (Supplementary Figs. 40 and 41). Such a solvent configuration can promote the formation of coordinated ion pairs and large-sized CIPAs. In contrast, for the LHCE-G3 electrolyte, the *gauche* peaks were blueshifted drastically (850 to 870 cm^{-1}) after adding LiFSI (Supplementary Fig. 40), revealing that the Li^+ ions coordinate to G3 primarily in the *gauche* configuration. The *gauche*-chelating configuration decreases the number of O atoms in the anions that can bind to Li^+ ions, suppressing the formation of CIPAs. The coordination state of the FSI^- anions in the first Li^+ solvation sheath was also studied by Raman spectroscopy, analysing the S–N–S stretching mode of the FSI^- anions (Supplementary Fig. 42). In the CIPA electrolyte, this band was entirely responsible for the AGG peak centred at ~745 cm^{-1}. This indicates that each anion is coordinated to more than two Li^+ ions, underlying the formation of CIPAs. The different solvation structures of the two electrolytes were also identified by ^{1}H and ^{7}Li NMR spectroscopy (Supplementary Figs. 43 and 44). The anion-rich first solvation sheath was quantified using the Li^+–O RDFs from MD simulations (Supplementary Figs. 45 and 46 and Supplementary Table 4). The RDFs show that the first solvation sheath of the CIPA electrolyte is dominated by anions with on average 2.56 O atoms, more than the O atoms contributed by EGBE (1.63). Such an anion-rich first solvation sheath could be beneficial for the prior reduction of FSI^- anions at the Li interface, forming the stable inorganic-rich SEI to rapidly terminate parasitic reactions and suppress solvent reduction. The projected electronic density of state (pDOS) profiles show that the conduction band of the anion in the CIPA electrolyte is lower than that of the solvents (Supplementary Figs. 47 and 48), suggesting preferential anion reduction.

Interfacial reaction mechanism

To understand the role of the CIPA electrolyte in SEI formation, we analysed the mechanisms of the reactions of the CIPA and LHCE-G3 electrolytes with Li metal through ab initio MD (AIMD) simulations over a timescale of 20 ps. Supplementary Fig. 49 shows representative MD snapshots. In the CIPA electrolyte, the preferential reduction of CIPAs was captured, while TTE did not react throughout the simulation. The reactions of the electrolyte components and their derivatives with the Li metal anode are shown in detail in Fig. 5. Notably, a group of FSI^- anions in the CIPA electrolyte underwent rapid reduction starting at 0.00, 0.69, 1.02 and 3.20 ps (Fig. 5a). This indicates that the CIPA electrolyte promotes rapid reduction kinetics of its anions via a collective electron-transfer mechanism, forming a SEI rich in inorganic compounds, including LiF and Li_2O, consistent with the TOF-SIMS and XPS analyses. In contrast, in the LHCE-G3 electrolyte, FSI^- did not react with Li during the simulation, while TTE underwent vigorous reduction (Fig. 5b). The different kinetic pathways for the decomposition of the CIPA and LHCE-G3 electrolytes eventually lead to the discrepancies in the SEI chemistry and structure discussed above. Importantly, the rapid collective reduction of the CIPA electrolyte effectively protects the Li metal through the rapid formation of a stable and thin SEI, substantially improving the battery performance.

Conclusions

We have designed and characterized a CIPA electrolyte to enable the stable cycling of 500 Wh kg^{-1} LMBs and understand its solvation structure and interfacial reaction mechanism. At the Li anode interface, multiple FSI^- anions in the CIPA electrolyte are rapidly reduced to form large amounts of LiF and Li_2O via a collective electron-transfer mechanism, forming a stable SEI with low organic content that effectively protects the Li metal anode from further side reactions. At the cathode interface, the CIPA electrolyte significantly reduces irreversible electrode change. The simultaneous stabilization of both the anode and cathode interfaces effectively mitigates electrolyte depletion, enabling the stable cycling of a 505.9 Wh kg^{-1} Li metal pouch cell over 130 cycles and ~2,750 h. This work showcases the importance of understanding electrolyte solvation structure and interfacial reaction mechanisms for realizing high-performance LMBs.

Methods

Materials

LiFSI, DME and TTE were obtained from Gthrchem, EGBE from Aladdin, G3 from DoDoChem and hydrochloric acid solution from Sinopharm. EGBE, G3, DME and TTE were stored over 4 Å molecular sieves overnight before use, and LiFSI was dried at 80 °C in a vacuum chamber overnight. The NCM811 cathode material was obtained from Ningde Amperex Technology. All of the chemicals were stored in a glove box filled with argon gas (O_2 < 1 ppm, H_2O < 1 ppm). The LiFSI–EGBE, LiFSI–G3, CIPA, LHCE-G3 and LHCE-DME electrolytes were prepared by directly adding 2 M LiFSI to EGBE, G3, EGBE–TTE (1:1, v/v), G3–TTE (1:1, v/v) and DME–TTE (1:1, v/v), respectively. The 4 M LiFSI–EGBE electrolyte was prepared by dissolving 4 M LiFSI in pure EGBE.

Electrochemical tests

All electrochemical tests, except for those on the Li metal pouch cells and GC–MS in situ cells, were conducted using 2032-type coin cells. The Li||Cu coin cells used to measure the CE of metallic Li plating/stripping and for SEM characterization of the plated Li comprised Li foil (450 µm, cellithium) with a diameter of 14 mm as the counter and reference electrodes, a polyethylene (PE) separator (16 µm) and copper foil (25 µm; Kejing MTI) as the working electrode. The Li||Cu coin cells for cryo-TEM characterization comprised Li foil (450 µm) as the counter and reference electrodes, a PE separator (16 µm) and a lacey carbon grid as the working electrode. Each coin cell was filled with 50 µl electrolyte. Li||NCM811 coin cells comprised Li foil (450 µm) as the anode, a PE separator (16 µm) and an NCM811 cathode (~2.5 mAh cm^{-2}, 1.13 cm^2). All cells were assembled inside a glove box (O_2 < 1 ppm, H_2O < 1 ppm). To fabricate the NCM811 cathode used in the coin cells, a slurry was

prepared by mixing the NCM811 material, poly(vinylidene fluoride) (PVDF; Keiing MTI) and Super P (Keiing MTI) in a mass ratio of 85:7.5:7.5 in *N*-methyl-2-pyrrolidone (NMP; Aladdin). The cathode slurry was then blade-coated onto carbon-coated aluminium foil (Kejing MTI) and dried at 80 °C overnight in a vacuum oven.

For the >500 Wh kg^{-1} Li metal pouch cells, Li foil (60 μm) was used as the anode and Ni90 as the cathode. To fabricate the Ni90 cathode, a slurry was prepared by mixing the Ni90 material, PVDF and carbon black in a mass ratio of 97:1.5:1.5 in NMP. The slurry was then spray-coated onto carbon-coated aluminium foil and dried at 100 °C overnight in a vacuum oven.

For the 423.7 Wh kg^{-1} Li metal pouch cells, Li foil (30 μm on each side) affixed to copper mesh was used as the anode and NCM811 as the cathode. To fabricate the NCM811 cathode, a slurry was prepared by mixing the NCM811 material, PVDF and carbon black in a mass ratio of 97:1.5:1.5 in NMP. The slurry was then spray-coated onto carbon-coated aluminium foil and dried at 80 °C overnight in a vacuum oven.

For the GC–MS in situ cells, Li foil (cellithium), a glass fibre separator (Whatman) and an NCM811 cathode (~2.5 mAh cm^{-2}) were used. A gas storage chamber was located inside the cells, separated by a metal inner wall, to collect the gases produced during battery cycling. The hole in gas storage chamber that connects to the external environment was blocked using rubber plugs.

Characterization of materials

Synchrotron-based WAXS data were collected on the BL16B1 beamline at Shanghai Synchrotron Radiation Facility (SSRF) using monochromatic X-rays with a beam energy of 10 keV and a beam size of 500 × 500 $μm^2$. The liquid samples were loaded into quartz capillaries (inner diameter 1.5 mm; Hampton), which were then sealed well and mounted on the sample stage. Signals were detected with a Pilatus 2M detector (1,475 × 1,679 pixels with 172 × 172 $μm^2$ $pixel^{-1}$) at a distance of 220 mm from the sample. The exposure time was 60 s for each sample. The two-dimensional patterns were exported and converted into one-dimensional diffraction intensity profiles as a function of wave vector Q using the Fit2D software (version 18)[48]. The raw data were then corrected by background scattering (an empty quartz capillary with air contribution), and structure factor function ($S(q)$) was extracted using the PDFgetX3 analysis package[49].

Synchrotron-based high-energy X-ray scattering data were collected on the BL12SCW beamline at SSRF using monochromatic X-rays with a beam energy of 88.6 keV and a beam size of 500 × 500 $μm^2$. The liquid samples were loaded into quartz capillaries (outer diameter 1.5 mm; Charles Supper), which were then sealed well and mounted on the sample stage. Signals were detected with a flat-type Pilatus3 2M CdTe detector (1,475 × 1,679 pixels with 172 × 172 $μm^2$ $pixel^{-1}$) at a distance of 245 mm from the sample in transmission geometry. The exposure time was 15 min for each sample. The geometry calibration and conversion of the two-dimensional patterns into one-dimensional diffraction intensity profiles as a function of Q were performed using the DIOPTAS software[50]. The raw data were then corrected by background subtraction (data were collected from an empty quartz capillary).

XPS was conducted with a Shimadzu Kratos AXIS SUPRA+ spectrometer equipped with an Al Kα source, an argon cluster ion sputtering gun and a high-vacuum transfer chamber. Samples were sealed in an airtight transfer container during the transfer process and opened after being loaded onto the stage inside the high-vacuum transfer chamber to prevent the exposure of samples to air. All of the spectra were calibrated with the C–C peaks centred at 284.8 eV. Depth-profiling experiments were carried out with argon cluster ion sputtering with a beam energy of 0.5 keV over an area of 2 × 2 mm^2.

Cryo-TEM was performed on a JEOL JEM-F200 microscope at a cryogenic temperature of −180 °C. The accelerating voltage for imaging was set at 200 kV. Li metal was plated onto lacey carbon grids in coin cells at 0.5 mA cm^{-2} for 30 min. The grids with the Li deposits were removed from the cells after the electrochemical process in an Ar-filled glove box and lightly rinsed with dimethyl carbonate to remove residual Li salts. The grids were then transferred to and sealed inside a cryo-TEM holder (Fischione 2550), which was placed inside another sealed airtight container to avoid air contamination during subsequent transfer. The cryo-TEM holder was then quickly and directly inserted into the microscope, which was then filled with liquid nitrogen to establish a stable temperature of −180 °C. Images were analysed using the Digital Micrograph (Gatan) software (version 3.52.3932.0).

SEM characterizations were performed using a FEI Apreo scanning electron microscope equipped with a Helios focused ion beam at an accelerating voltage of 2 kV. All samples consisted of Cu foil with Li deposits, collected from Li||Cu coin cells disassembled in an Ar-filled glove box after galvanostatic plating at 0.5 mA cm^{-2}. The Li-plated Cu foils were rinsed with DME to remove residual Li salts. The washed samples were dried and placed inside a sealed container in the glove box before loading onto the sample stage within 10 s.

FIB-SEM cross-section views of NCM811 cathodes were obtained on a FEI Helios 600i microscope operated at 2–30 kV. The NCM811 particles were collected from disassembled cycled Li||NCM811 cells and milled to about 100 nm using a Ga^+ ion beam. HAADF-STEM characterization was performed using a FEI Titan G2 60-300 microscope at an accelerating voltage of 300 kV. The microscope was equipped with a spherical aberration corrector to enable sub-ångstrom imaging when using HAADF-STEM detectors.

ICP-MS was performed on a Thermo Fisher iCAP RQ spectrometer to measure transition metal dissolution from the cycled NCM811 cathode. Samples were prepared by dissolving the Li metal anodes with deposited transition metals from cycled Li||NCM811 cells (2.8–4.3 V, 0.5 C/1 C, 50 cycles). First, 1 ml deionized water was added to a bottle containing the cycled Li, followed by 1 ml hydrochloric acid solution and 8 ml deionized water to yield a transparent solution for analysis.

GC–MS was performed on a Shimadzu Nexis GC-2030 spectrometer. A gas-tight syringe was used to transfer 50 μl of the gases from the in situ cells to the GC system after a charge/discharge cycle (2.8–4.3 V, 0.1 C/0.1 C). The gases mixed with helium (99.9999%) carrier gas at a total gas flow rate of 8.07 ml min^{-1} were analysed using a barrier ionization discharge (BID) detector. The MICROPACKED-ST column used for chromatographic separation was maintained at 35 °C and the BID detector at 280 °C. The split ratio was kept at 5:1 and the split temperature at 250 °C.

TOF-SIMS was performed on a TOF.SIMS5-100 spectrometer equipped with a 1 keV Cs^+ ion beam for sputtering. Samples were analysed using a 10 keV Bi^+ ion beam over an area of 100 × 100 $μm^2$. Samples for analysis were prepared by plating Li onto Cu substrates (3 mAh cm^{-2}) in Li||Cu cells. All Li||Cu cells for sample preparation were disassembled and washed in a glove box under an argon atmosphere. Then the samples were transferred to the stage of the spectrometer inside the glove box without being exposed to air.

The solvation structure of the electrolytes was examined by Raman spectroscopy using a Renishaw inVia Raman microscope. The electrolytes were sealed inside flat airtight quartz capillaries with high light transmittance in a glove box, which were subsequently loaded onto the sample stage. The wavelength of the incident laser was 532 nm and the exposure time was 2 s with 30 accumulations.

NMR analysis was performed on a Bruker JNM-ECZ600R/S1 600 MHz NMR spectrometer. CIPA, LHCE-G3, LiFSI–EGBE and LiFSI–G3 electrolytes and TTE solution were sealed in airtight NMR tubes and loaded onto the sample stage for analysis.

Differential scanning calorimetry (DSC) was performed using a TA Instruments DSC Q2000 calorimeter. Each sample (~13 mg) was sealed in a crimp-sealed holder for analysis. The cooling/heating rate was set at 5 °C min^{-1}.

Theoretical calculations

Snapshots of solvation structures and RDFs were derived from classical molecular dynamics (cMD) simulations performed using GROMACS (2020.1)[51]. Before carrying out the cMD simulations, the intramolecular force field parameters were optimized using optimized geometries and the Hessian matrix with the Perdew–Burke–Ernzerhof (PBE) functional and 6-31+G* basis set using Jaguar (version 8.8)[52]. The simulation models were built in accord with the experimental composition, that is, 132 LiFSI, 186 TTE molecules and 132 EGBE molecules randomly placed in a periodic box with a volume of 111.98 nm^3. After geometry optimization, the simulations were first equilibrated for 1.0 ns at 300 K using the canonical (NVT) ensemble in which the number of particles (N), cell volume (V) and temperature (T) are all kept fixed, then for 2.0 ns controlling the pressure at 1 bar using the isothermal–isobaric (NPT) ensemble in which the number of particles (N), pressure (P) and temperature (T) are all kept fixed, and finally for 1.0 ns under NVT conditions using averaged cell parameters from the NPT simulation. Temperature coupling was performed using velocity rescaling (V-rescale) with a stochastic term and a 0.1 ps time constant. Berendsen pressure coupling was performed with a time constant of 0.5 ps.

The pDOS calculations were performed using the Vienna Ab initio Simulation Package (VASP, version 5.4.4)[53] and the projector augmented wave method[54] with a plane-wave basis set. Generalized gradient approximations of the PBE functional were adopted[55]. The $3s^23p^4$, $2s^22p^5$, $2s^22p^4$, $2s^22p^3$, $2s^22p^2$, $2s^1$ and $1s^1$ valence electrons were treated explicitly for S, F, O, N, C, Li and H, respectively. The density functional theory D3 method with Becke–Johnson damping was included for dispersion correction[56]. A 400 eV energy cut-off was set with no consideration of spin polarization in the calculations. The reciprocal space was sampled using the Γ-centred Monkhorst–Pack scheme[57] with a 3 × 3 × 1 grid. The partial occupancies of each orbital were set in the first-order Methfessel–Paxton scheme with a smearing width of 0.2 eV. The dipole moment corrections for total energy were applied along the surface's normal direction. For the self-consistent electronic step, convergence was set at a threshold of 10^{-4} eV for changes in total energy.

NVT AIMD simulations were performed at 300 K using a Nosé–Hoover thermostat with a damping parameter of 200 fs. A 1 fs time step was used with the mass of hydrogen set to 2 atomic mass units. The velocities were scaled to the targeted temperature every 20 steps for equilibration. In the investigation of the reactions between the CIPA electrolyte and the Li metal anode, the solvation effect was included using the implicit solvation model as implemented in VASPsol (ref. 58) and the applied potential was controlled at $U = 0$ V versus Li^+/Li by the open-source subroutine TPOT (ref. 59). The initial models of the CIPA and LHCE solvation structures were obtained from cMD simulations.

Data availability

All of the data that support the findings of this study are available in the main text and Supplementary Information. Source data are provided with this paper.

Code availability

The MD simulation codes used in this work are available at https://doi.org/10.6084/m9.figshare.25906249.v1 (ref. 60).

References

1. Lin, D., Liu, Y. & Cui, Y. Reviving the lithium metal anode for high-energy batteries. *Nat. Nanotechnol.* **12**, 194–206 (2017).
2. Liu, J. et al. Pathways for practical high-energy long-cycling lithium metal batteries. *Nat. Energy* **4**, 180–186 (2019).
3. Louli, A. J. et al. Diagnosing and correcting anode-free cell failure via electrolyte and morphological analysis. *Nat. Energy* **5**, 693–702 (2020).
4. Meng, Y. S., Srinivasan, V. & Xu, K. Designing better electrolytes. *Science* **378**, eabq3750 (2022).
5. Yu, Z. et al. Rational solvent molecule tuning for high-performance lithium metal battery electrolytes. *Nat. Energy* **7**, 94–106 (2022).
6. Wan, H., Xu, J. & Wang, C. Designing electrolytes and interphases for high-energy lithium batteries. *Nat. Rev. Chem.* **8**, 30–44 (2024).
7. Fan, X. et al. Non-flammable electrolyte enables Li-metal batteries with aggressive cathode chemistries. *Nat. Nanotechnol.* **13**, 715–722 (2018).
8. Niu, C. et al. High-energy lithium metal pouch cells with limited anode swelling and long stable cycles. *Nat. Energy* **4**, 551–559 (2019).
9. Jie, Y. et al. Molecular understanding of interphase formation via operando polymerization on lithium metal anode. *Cell Rep. Phys. Sci.* **3**, 101057 (2022).
10. Qian, J. et al. High rate and stable cycling of lithium metal anode. *Nat. Commun.* **6**, 6362 (2015).
11. Fan, X. et al. Highly fluorinated interphases enable high-voltage Li-metal batteries. *Chem* **4**, 174–185 (2018).
12. Rustomji, C. S. et al. Liquefied gas electrolytes for electrochemical energy storage devices. *Science* **356**, eaal4263 (2017).
13. Yang, Y. et al. High-efficiency lithium-metal anode enabled by liquefied gas electrolytes. *Joule* **3**, 1986–2000 (2019).
14. Yin, Y. et al. Fire-extinguishing, recyclable liquefied gas electrolytes for temperature-resilient lithium-metal batteries. *Nat. Energy* **7**, 548–559 (2022).
15. Yu, Z. et al. Molecular design for electrolyte solvents enabling energy-dense and long-cycling lithium metal batteries. *Nat. Energy* **5**, 526–533 (2020).
16. Chen, S. et al. High-voltage lithium-metal batteries enabled by localized high-concentration electrolytes. *Adv. Mater.* **30**, 1706102 (2018).
17. Ren, X. et al. Localized high-concentration sulfone electrolytes for high-efficiency lithium-metal batteries. *Chem* **4**, 1877–1892 (2018).
18. Fan, X. et al. All-temperature batteries enabled by fluorinated electrolytes with non-polar solvents. *Nat. Energy* **4**, 882–890 (2019).
19. Kim, S. C. et al. High-entropy electrolytes for practical lithium metal batteries. *Nat. Energy* **8**, 814–826 (2023).
20. Zhang, W. et al. Single-phase local-high-concentration solid polymer electrolytes for lithium-metal batteries. *Nat. Energy* **9**, 386–400 (2024).
21. Wu, Z. et al. Deciphering and modulating energetics of solvation structure enables aggressive high-voltage chemistry of Li metal batteries. *Chem* **9**, 650–664 (2023).
22. Zhao, Y. et al. Electrolyte engineering for highly inorganic solid electrolyte interphase in high-performance lithium metal batteries. *Chem* **9**, 682–697 (2023).
23. Ren, X. et al. Role of inner solvation sheath within salt–solvent complexes in tailoring electrode/electrolyte interphases for lithium metal batteries. *Proc. Natl Acad. Sci. USA* **117**, 28603–28613 (2020).
24. Cao, X. et al. Effects of fluorinated solvents on electrolyte solvation structures and electrode/electrolyte interphases for lithium metal batteries. *Proc. Natl Acad. Sci. USA* **118**, e2020357118 (2021).
25. Niu, C. et al. Balancing interfacial reactions to achieve long cycle life in high-energy lithium metal batteries. *Nat. Energy* **6**, 723–732 (2021).
26. Lin, L. et al. Li-rich $Li_2[Ni_{0.8}Co_{0.1}Mn_{0.1}]O_2$ for anode-free lithium metal batteries. *Angew. Chem. Int. Ed.* **60**, 8289–8296 (2021).
27. Deng, W. et al. Competitive solvation-induced concurrent protection on the anode and cathode toward a 400 Wh kg^{-1} lithium metal battery. *ACS Energy Lett.* **6**, 115–123 (2021).
28. Ma, Q. et al. Formulating the electrolyte towards high-energy and safe rechargeable lithium-metal batteries. *Angew. Chem. Int. Ed.* **60**, 16554–16560 (2021).

29. Zhang, X.-Q. et al. A sustainable solid electrolyte interphase for high-energy-density lithium metal batteries under practical conditions. *Angew. Chem. Int. Ed.* **59**, 3252–3257 (2020).
30. Gao, Y. et al. Multifunctional silanization interface for high-energy and low-gassing lithium metal pouch cells. *Adv. Energy Mater.* **10**, 1903362 (2020).
31. Zhang, K. et al. A high-performance lithium metal battery with ion-selective nanofluidic transport in a conjugated microporous polymer protective layer. *Adv. Mater.* **33**, 2006323 (2021).
32. Xu, Q. et al. High energy density lithium metal batteries enabled by a porous graphene/MgF_2 framework. *Energy Storage Mater.* **26**, 73–82 (2020).
33. Huang, K. et al. Regulation of SEI formation by anion receptors to achieve ultra-stable lithium-metal batteries. *Angew. Chem. Int. Ed.* **60**, 19232–19240 (2021).
34. Martin, C., Genovese, M., Louli, A. J., Weber, R. & Dahn, J. R. Cycling lithium metal on graphite to form hybrid lithium-ion/lithium metal cells. *Joule* **4**, 1296–1310 (2020).
35. Kim, J.-H., Kim, J.-M., Cho, S.-K., Kim, N.-Y. & Lee, S.-Y. Redox-homogeneous, gel electrolyte-embedded high-mass-loading cathodes for high-energy lithium metal batteries. *Nat. Commun.* **13**, 2541 (2022).
36. Gao, Y. et al. Effect of the supergravity on the formation and cycle life of non-aqueous lithium metal batteries. *Nat. Commun.* **13**, 5 (2022).
37. Ou, X. et al. Enabling high energy lithium metal batteries via single-crystal Ni-rich cathode material co-doping strategy. *Nat. Commun.* **13**, 2319 (2022).
38. Shangguan, X. et al. Additive-assisted novel dual-salt electrolyte addresses wide temperature operation of lithium-metal batteries. *Small* **15**, 1900269 (2019).
39. Lin, L. et al. Epitaxial induced plating current-collector lasting lifespan of anode-free lithium metal battery. *Adv. Energy Mater.* **11**, 2003709 (2021).
40. Zhao, P. et al. Constructing self-adapting electrostatic interface on lithium metal anode for stable 400 Wh kg^{-1} pouch cells. *Adv. Energy Mater.* **12**, 2200568 (2022).
41. Zhang, Q.-K. et al. Homogeneous and mechanically stable solid-electrolyte interphase enabled by trioxane-modulated electrolytes for lithium metal batteries. *Nat. Energy* **8**, 725–735 (2023).
42. Mao, M. et al. Anion-enrichment interface enables high-voltage anode-free lithium metal batteries. *Nat. Commun.* **14**, 1082 (2023).
43. Chang, Z., Yang, H., Pan, A., He, P. & Zhou, H. An improved 9 micron thick separator for a 350 Wh/kg lithium metal rechargeable pouch cell. *Nat. Commun.* **13**, 6788 (2022).
44. Shi, P. et al. Inhibiting intercrystalline reactions of anode with electrolytes for long-cycling lithium batteries. *Sci. Adv.* **8**, eabq3445 (2022).
45. Xia, Y. et al. Designing an asymmetric ether-like lithium salt to enable fast-cycling high-energy lithium metal batteries. *Nat. Energy* **8**, 934–945 (2023).
46. Roik, O. S., Samsonnikov, O. V., Kazimirov, V. P., Sokolskii, V. E. & Galushko, S. M. Medium-range order in Al-based liquid binary alloys. *J. Mol. Liq.* **151**, 42–49 (2010).
47. Wada, R., Fujimoto, K. & Kato, M. Why is poly(oxyethylene) soluble in water? Evidence from the thermodynamic profile of the conformational equilibria of 1,2-dimethoxyethane and dimethoxymethane revealed by Raman spectroscopy. *J. Phys. Chem. B* **118**, 12223–12231 (2014).
48. Hammersley, A. P. FIT2D: a multi-purpose data reduction, analysis and visualization program. *J. Appl. Cryst.* **49**, 646–652 (2016).
49. Juhás, P., Davis, T., Farrow, C. L. & Billinge, S. J. L. PDFgetX3: a rapid and highly automatable program for processing powder diffraction data into total scattering pair distribution functions. *J. Appl. Cryst.* **46**, 560–566 (2013).
50. Prescher, C. & Prakapenka, V. B. DIOPTAS: a program for reduction of two-dimensional X-ray diffraction data and data exploration. *High. Press. Res.* **35**, 223–230 (2015).
51. Abraham, M. J. et al. GROMACS: high performance molecular simulations through multi-level parallelism from laptops to supercomputers. *SoftwareX* **1**, 19–25 (2015).
52. Jaguar, version 8.8 (Schrödinger, LLC, 2015).
53. Kresse, G. & Hafner, J. Ab initio molecular-dynamics simulation of the liquid-metal–amorphous-semiconductor transition in germanium. *Phys. Rev. B* **49**, 14251–14269 (1994).
54. Kresse, G. & Joubert, D. From ultrasoft pseudopotentials to the projector augmented-wave method. *Phys. Rev. B* **59**, 1758–1775 (1999).
55. Perdew, J. P., Burke, K. & Ernzerhof, M. Generalized gradient approximation made simple. *Phys. Rev. Lett.* **77**, 3865–3868 (1996).
56. Naserifar, S. et al. Accurate non-bonded potentials based on periodic quantum mechanics calculations for use in molecular simulations of materials and systems. *J. Chem. Phys.* **151**, 154111 (2019).
57. Monkhorst, H. J. & Pack, J. D. Special points for Brillouin-zone integrations. *Phys. Rev. B* **13**, 5188–5192 (1976).
58. Mathew, K., Sundararaman, R., Letchworth-Weaver, K., Arias, T. A. & Hennig, R. G. Implicit solvation model for density-functional study of nanocrystal surfaces and reaction pathways. *J. Chem. Phys.* **140**, 084106 (2014).
59. Le, D. An explicit-implicit hybrid solvent model for grand canonical simulations of the electrochemical environment. Preprint at *ChemRxiv* https://doi.org/10.26434/chemrxiv-2023-z2n4n (2023).
60. Liu, Y. & Cheng, T. Simulation data for compact ion-pair aggregate electrolyte. *figshare* https://doi.org/10.6084/m9.figshare.25906249.v1 (2024).

Acknowledgements

S.J. acknowledges the support of the National Natural Science Foundation of China (grant no. 52225105). D.X., S.J., R.C., Y.J., T.C., Y. Liu and X.W. thank the National Key Research and Development Program of China (grant nos. 2022YFA1504102 and 2022YFB2502200), the Strategic Priority Research Program of the Chinese Academy of Sciences (grant no. XDB0450302) and the National Natural Science Foundation of China (grant nos. 22279127, 52072358, U21A2082, 21821004, 22309173, 22173066 and 22303058). S.J. and R.C. also appreciate the financial support of Gotion High Tech Co. Synchrotron-based WAXS was conducted on the BL16B1 beamline at the SSRF, and we acknowledge F. Bian and X. Miao for conducting WAXS experiments and analysing the data. Synchrotron-based high-energy X-ray scattering experiment was conducted on the BL12SCW beamline at the SSRF, and we acknowledge Z. Luo for discussion and data analysis. We acknowledge M. Gu and M. Li for the discussion on cryo-TEM characterizations. Material characterizations in this work were partially carried out at the Instruments Center for Physical Science, University of Science and Technology of China. The computational calculations were partially done on the supercomputing system in the Supercomputing Center of the University of Science and Technology of China.

Author contributions

D.X. and S.J. designed the project and conceptualized the idea. Y.J., S. Wang, X.L. and F.H. performed the SEM and XPS characterizations, electrochemical experiments and coin-cell tests. S. Weng and X.W. conducted the cryo-TEM and TOF-SIMS characterizations. Y. Liu and T.C. performed the MD simulations. M.Y. and C.T. performed the pouch cell tests. Z.Z. and P.Y. conducted the STEM experiments. S.C., Y.J., H.L. and K.Y. performed the synchrotron-based high-energy X-ray scattering tests. All authors discussed and analysed the data. Y.J., Y.X., R.C., T.C., X.W., S.J. and D.X. wrote and revised the paper.

Competing interests
The authors declare no competing interests.

Additional information
Supplementary information The online version contains supplementary material available at https://doi.org/10.1038/s41560-024-01565-z.

Correspondence and requests for materials should be addressed to Tao Cheng, Xuefeng Wang, Shuhong Jiao or Dongsheng Xu.

Peer review information *Nature Energy* thanks Steve Greenbaum, Tomas Rojas and the other, anonymous, reviewer(s) for their contribution to the peer review of this work.

[1]Hefei National Laboratory for Physical Science at the Microscale, CAS Key Laboratory of Materials for Energy Conversion, Department of Materials Science and Engineering, University of Science and Technology of China, Hefei, China. [2]Beijing National Laboratory for Molecular Sciences, College of Chemistry and Molecular Engineering, Peking University, Beijing, China. [3]National Laboratory for Condensed Matter Physics, Institute of Physics, Chinese Academy of Sciences, Beijing, China. [4]Institute of Functional Nano and Soft Materials, Jiangsu Key Laboratory for Carbon-Based Functional Materials and Devices, Jiangsu Key Laboratory of Advanced Negative Carbon Technologies, Soochow University, Suzhou, China. [5]Science and Technology on Power Sources Laboratory, Tianjin Institute of Power Sources, Tianjin, China. [6]Ningde Amperex Technology, Ningde, China. [7]Beijing Key Laboratory of Microstructure and Properties of Solids, Faculty of Materials and Manufacturing, Beijing University of Technology, Beijing, China. [8]Institute of Electrochemical Energy Storage, Helmholtz-Zentrum Berlin für Materialien und Energie, Berlin, Germany. [9]Shanghai Advanced Research Institute, Chinese Academy of Sciences, Shanghai, China. [10]Tianmu Lake Institute of Advanced Energy Storage Technologies, Liyang, China. [11]These authors contributed equally: Yulin Jie, Shiyang Wang, Suting Weng, Yue Liu. ✉e-mail: tcheng@suda.edu.cn; wxf@iphy.ac.cn; jiaosh@ustc.edu.cn; dsxu@pku.edu.cn